ChemPhysMater 3 (2024) 74–82

Contents lists available at ScienceDirect

ChemPhysMater

journal homepage: https://www.keaipublishing.com/en/journals/chemphysmater/

Research Article

Mo-doped one-dimensional needle-like Ni_3S_2 as bifunctional electrocatalyst for efficient alkaline hydrogen evolution and overall-water-splitting

Junjie Huang[#], Yupeng Xing[#], Jinzhao Huang, Fei Li, Gang Zhao[*], Xingmin Yu, Binxun Li, Xinran Zhang

School of Physics and Technology, University of Jinan, Jinan 250022, China

ARTICLE INFO

Keywords:
Hydrogen evolution reaction
Molybdenum doped
Nickel sulfide
Overall water splitting
Needle-like multistage structure

ABSTRACT

Hydrogen energy plays an important role in clean energy system and is considered the core energy source for future technological development owing to its lightweight nature, high calorific value, and clean combustion products. The electrocatalytic conversion of water into hydrogen is considered a highly promising method. An electrocatalyst is indispensable in the electrocatalytic process, and finding an efficient electrocatalyst is essential. However, the current commercial electrocatalysts (such as Pt/C and Ru) are expensive; therefore, there is a need to find an inexpensive and efficient electrocatalyst with high stability, corrosion resistance, and high electrocatalytic efficiency. In this study, we developed a cost-effective bifunctional electrocatalyst by incorporating molybdenum into nickel sulfide (Ni_3S_2) and subsequently tailoring its structure to achieve a one-dimensional (1D) needle-like configuration. The hydrogen production efficiency of nickel sulfide was improved by changing the ratio of Mo doping. By analyzing the electrochemical performance of different Mo-doped catalysts, we found that the Ni_3S_2-Mo-0.1 electrocatalyst exhibited the best electrocatalytic effect in 1 M KOH; at a current density of 10 mA cm^{-2}, it exhibited overpotentials of 120 and 279 mV for hydrogen evolution reaction (HER) and oxygen evolution reaction (OER), respectively; at a higher current density of 100 mA cm^{-2}, the HER and OER overpotentials were 396 and 495 mV, respectively. Furthermore, this electrocatalyst can be used in a two-electrode water-splitting system. Finally, we thoroughly investigated the mechanism of the overall water splitting of this electrocatalyst, providing valuable insights for future hydrogen production via overall-water-splitting.

1. Introduction

Currently, the Earth's climate is deteriorating owing to the extensive utilization of fossil fuels[1]. Issues such as the greenhouse effect and energy crisis are becoming increasingly serious. Simultaneously, the global population is expanding, leading to a surge in energy requirements [2–4]. However, fossil fuels are limited. Hence, there is an urgent need to identify sustainable and clean energy sources [5,6]. Hydrogen has garnered significant interest as a promising environmentally friendly energy source owing to its high energy density and nontoxic nature, as its sole by-product is water upon combustion. This combustion process prevents the release of hazardous or deleterious compounds, ensuring a minimal environmental impact [7–9]. Therefore, hydrogen production by the electrolysis of water, in which water is split into hydrogen and oxygen using electrical energy, has become a research focus for numerous researchers [10–15].

Currently, commercial catalysts such as Pt-based noble metals and IrO_2/RuO_2 are not suitable for large-scale applications owing to their limited reserves and high costs [16–18]. Consequently, the development of cost-effective and high-efficiency electrocatalysts for the overall water splitting process is of great significance. Amidst these options, transition metal sulphides have the advantages of superior theoretical catalytic performance, low cost, and abundant reserves [19,20]. Ni_3S_2, which has abundant active sites and exhibits high catalytic activity in electrocatalytic water splitting, can reduce the overpotentials for efficient alkaline hydrogen production and complete water splitting. Ni_3S_2 exhibits excellent electrical conductivity, high theoretical capacitance, low cost, and high redox efficiency. However, for practical applications, the rational design and easy preparation of Ni_3S_2 with high electrochemical properties continue to pose significant challenges. Despite the considerable potential of Ni_3S_2 in the field of electrocatalysis, further research is essential to completely understand its electrocatalytic mechanisms and fine-tune its performance. Pure Ni_3S_2 has a strong adsorption capacity for water-splitting intermediates owing to strong S–Ni bonds, which hinder proton desorption, ultimately resulting in reduced electrocatalytic performance [21–24]. To optimize the adsorption capacity

* Corresponding author.
E-mail address: sps_zhaog@ujn.edu.cn (G. Zhao).
# These authors contributed equally to this work.

https://doi.org/10.1016/j.chphma.2023.11.001
Received 31 August 2023; Received in revised form 1 November 2023; Accepted 2 November 2023
Available online 20 November 2023

of the overall water-splitting intermediates on the Ni_3S_2 surface, effective strategies must be developed. The incorporation of heteroatoms to modulate the electronic configuration of the Ni_3S_2 surface is a viable approach for enhancing the electrocatalytic efficiency [25,26]. Molybdenum has many advantages; for example, the introduction of Mo can add more catalytically active sites to the electrode, increase the electron transfer rate, diminish the oxidation reaction at the nickel sulfide electrode, and suppress the creation of oxides on the electrode surface, ultimately resulting in a significant reduction in the corrosion rate of the material. Therefore, we introduced molybdenum, which has a lower electron affinity energy and higher electrical conductivity (1.87×10^7 S m^{-1}) [27–31].

Herein, we successfully synthesized Mo-doped Ni_3S_2-Mo electrocatalysts using a one-step hydrothermal method with the aim of achieving complete catalytic hydrolysis. The experimental findings indicate that the Mo-doped Ni_3S_2-Mo electrocatalyst possessed excellent electrical conductivity, ample active sites, efficient electron transport pathways, and enhanced electrocatalytic effect. Notably, the Ni_3S_2-Mo-0.1 electrode demonstrated remarkable hydrogen production capability in a 1 M KOH alkaline environment, attaining a current density of 10 mA cm^{-2} with a low overpotential (HER of 120 mV). Simultaneously, it also shows impressive OER performance, with the same current density achieved at a low overpotential (OER of 279 mV). Furthermore, both materials exhibited excellent long-term stability in 1 M KOH, with an overpotential drop of only 1 mV after 12 h of continuous operation. We then constructed an overall water-splitting system using two Ni_3S_2-Mo-0.1 electrodes and tested their long-term stability. The results showed that a voltage of 1.62 V was required to achieve overall water splitting at a current density of 10 mA cm^{-2}. In conclusion, a high-performance 1D needle-like Mo-doped nickel sulfide bifunctional electrocatalyst (Ni_3S_2-Mo-0.1) was successfully prepared. This study introduces a feasible strategy for the prospective structural design of electrocatalysts [32,33].

2. Experimental section

2.1. Materials

Thiourea (CH_4N_2S), acetone (C_3H_6O), and ethanol (C_2H_5OH) were purchased from Sinopharm Chemical Reagent Co. Sodium molybdate (Na_2MoO_4) was purchased from Damo Chemical Reagent Factory (Tianjin, China). Nickel foam (Ni foam) was purchased from Ce Tech Co. All the chemical reagents were used directly without further purification. All solutions used in this study were formulated using deionized water with a resistivity of 18 MΩ.

2.2. Pretreatment of nickel foam

Ni foam was cut into 2 cm × 3 cm using a cutter, and its surface was washed with deionized water to remove impurities and other contaminants. The samples were sequentially ultrasonicated in acetone, ethanol, and deionized water to remove the deeper impurities. After the completion of the above operations, the nickel foam underwent a drying process in a vacuum oven maintained at 60 °C, for 6 h.

2.3. Preparation of Ni_3S_2-Mo composite catalytic electrode

The preparation of Ni_3S_2-Mo was carried out via single-step hydrothermal synthesis. 0.12 g of CH_4N_2S and 0.1 g of Na_2MoO_4 were dissolved in 30 mL deionized water and stirred with a magnetic stirrer for 3 h to obtain a solution. The solution was then transferred to an autoclave in a 2 cm × 3 cm of nickel foam for hydrothermal reaction and heated at 200 °C for 7 h. The sample of Ni_3S_2-Mo was collected and vacuum-dried at 60 °C for 6 h. The Ni_3S_2-Mo sample was acquired. Subsequently, it was subjected to vacuum drying at a temperature of 60 °C for 6 h.

2.4. Electrochemical measurements

Electrochemical measurements were performed using a CHI760E workstation with a conventional three-electrode configuration in a 1 M KOH electrolyte solution to assess the electrocatalytic traits. Ni_3S_2-Mo was directly employed as the working electrode, a platinum sheet served as the counter electrode, and Ag/AgCl (3 M KCl) served as the reference electrode. All tests were performed at room temperature (20 °C). The capacitive current exhibited a decrement when the scan rate was set at 1 mV/s, with an iR compensation applied in the range of −2 to 1. The complete linear scanning voltammetry (LSV) characteristics of the tests were recorded, and the results were calibrated using the Nernst equation as follows:

$$E(\text{vs.RHE}) = E(\text{vs.Ag/AgCl}) + \left(\frac{0.0592}{n}\right)\lg\frac{C^0}{C_\alpha^0},$$

$$4OH^- - 4e^- = O_2 + 2H_2O,$$

$$2H^+ + 2e^- = H_2,$$

$$\text{pH} = -\lg[H^+] = \lg\frac{1}{[H^+]},$$

$$E(\text{vs.RHE}) = E(\text{vs.Ag/AgCl}) + 0.0592 \times \text{pH},$$

$$E_{\text{HER}}(\text{vs.RHE}) = E(\text{vs.Ag/AgCl}) + 1.023.$$

Based on the oxygen reduction reaction, the initial potential of the OER is 1.23 V,

$$E_{\text{OER}}(\text{vs.RHE}) = E(\text{vs.Ag/AgCl}) + 1.023 - 1.23 = E(\text{vs.Ag/AgCl}) - 0.207.$$

In Tafel data, the horizontal coordinate is log $|A|$, where A is the overpotential obtained after the Nernst calibration. Cyclic voltammetry (CV) was used to evaluate the electrochemical double layer capacitance (C_{dl}) in the non-Faraday range (0.12–0.22 V vs. RHE) to assess the electrochemically active surface area (ECSA) of each sample [34,35]. The CV scan rates ranged from ~20–120 mV s^{-1} in increments of 20 mV s^{-1}. A graphical representation was formulated by plotting the current densities against the scan rates, using 0.2 V as the ordinate and the scan rate as the abscissa. The frequency range for the electrochemical impedance spectroscopy (EIS) was 100 kHz to 0.01 Hz. Ni_3S_2-Mo-0.1 electrodes were assigned as both cathode and anode, thereby constituting a two-electrode configuration. The capacity of the system to decompose water was then assessed.

3. Results and discussion

3.1. Synthesis and characterizations of the electrocatalysts

Fig. 1 shows the synthesis of different Ni_3S_2-Mo samples in which the addition of doped sodium molybdate was 0, 0.05, 0.1, and 0.15 g. By adjusting the quantity of sodium molybdate, three electrocatalysts with different morphologies on the surface of nickel foam were successfully prepared. The microstructures of the three electrocatalysts were examined using scanning electron microscopy (SEM) at various magnifications to gain insights into their structural features. As shown in Fig. S1, pristine nickel foam had many small pores and channels, which improved the contact area of the electrode with the electrolyte and simultaneously provided raw material for the formation of nickel sulfide (Ni_3S_2). After the one-step hydrothermal treatment, the material uniformly covered the surface of the nickel, as shown in Fig. 2. The surface of Ni_3S_2-Mo-0 showed stacked spherical structures (Fig. 2(a)). However, the morphologies of the Ni_3S_2-Mo electrocatalysts, doped with different quantities of sodium molybdate (Na_2MoO_4), underwent significant changes. For instance, the material morphology in Fig. 2(b) showed entangled fibrous filaments, while Fig. 2(c) displayed 1D needle-like structures, and Fig. 2(d) featured long nanorods. The doping of molybdenum atoms transformed the morphology of the catalyst from spherical to 1D needle-like structures, which exposed more active sites.

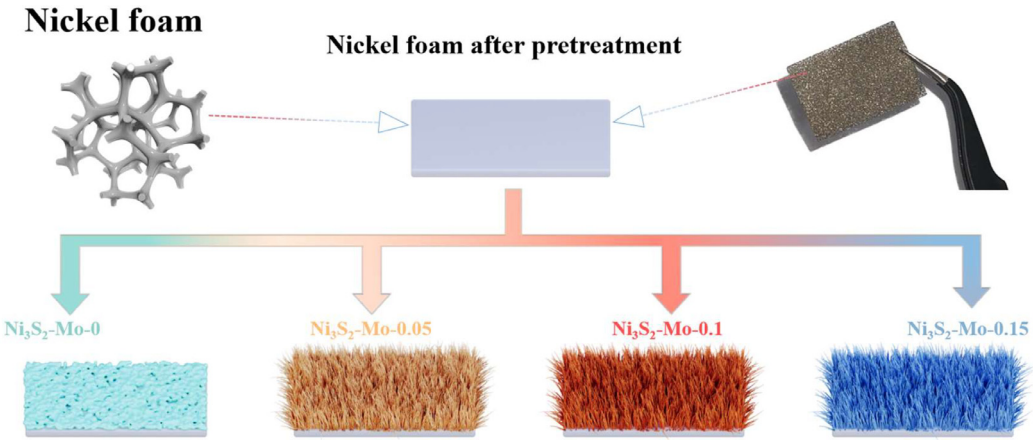

Fig. 1. Flowchart of material synthesis for different samples.

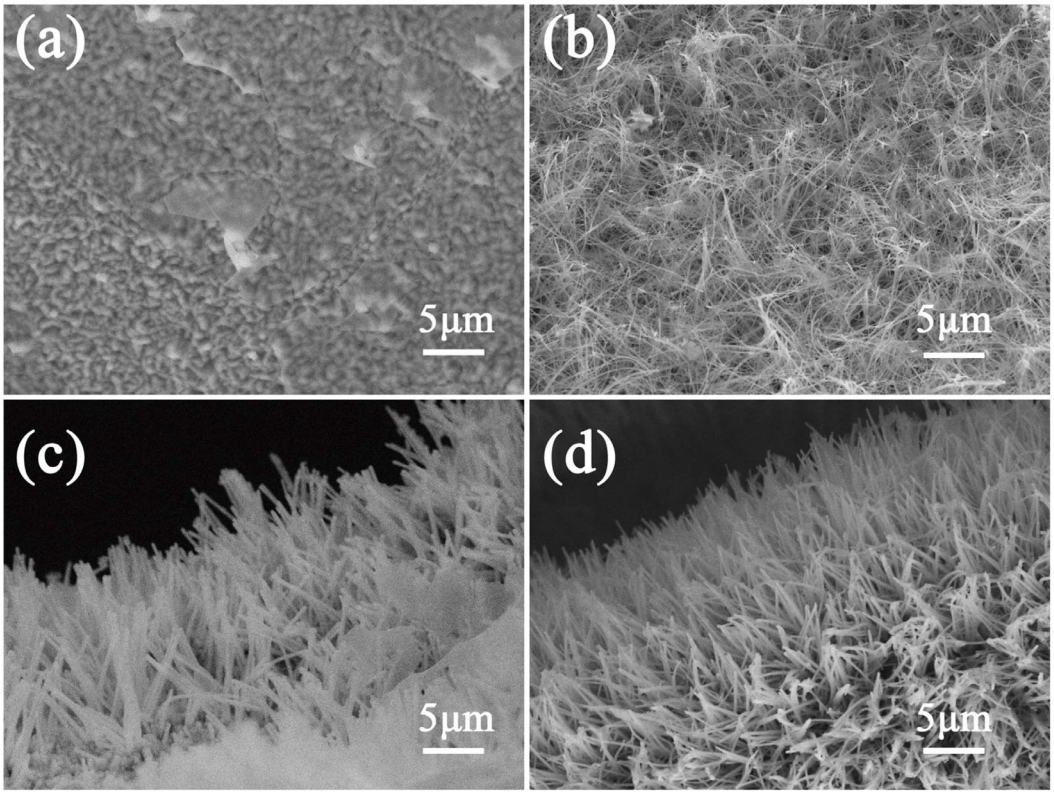

Fig. 2. SEM images of (a) Ni_3S_2-Mo-0, (b) Ni_3S_2-Mo-0.05, (c) Ni_3S_2-Mo-0.1, and (d) Ni_3S_2-Mo-0.15.

Ni_3S_2-Mo-0.1 has a one-dimensional needle-like structure, which manifest as a bundle of elongated fibers, and the lengths of the fibers vary between a few micrometers and tens of micrometers. The formation of one-dimensional fibers can be attributed to the orientation of the surfactant during the growth process, which lead to the elongated morphology of the nanorods.

In Fig. 3(a), Ni_3S_2-Mo-0.1 shows 1D needle-like structures, consistent with the SEM image, while Figs. 3(b)(c) show fragmented Ni_3S_2-Mo-0.1. In Figs. 3(d)(e), a set of lattice stripes with a spacing of 0.209 nm, corresponding to the (021) crystal surface of Ni_3S_2 (PDF #44-1418), and another set of lattice strips with a spacing of 0.178 nm, corresponding to the (110) crystallographic plane of Ni_3S_2 (PDF#44-1418), were observed. The presence of clear boundaries between these two sets of lattice stripes suggests that thiourea and nickel foam were successfully used to synthesize Ni_3S_2. The overall lattice stripes of the material were clearly visible, indicating a high degree of crystallinity. An Energy-dispersive X-ray spectroscopy (EDS) mapping confirmed that the prepared samples were primarily composed of three elements, namely S, Mo, and Ni (Figs. 3(f)–(i)).

The X-ray diffraction (XRD) analyses were conducted on each sample to acquire insights into the physical phases of each specimen, and the results are presented in Fig. 4(a). The distinctive diffraction peaks observed at 44.3°, 51.8°, and 76.3° align with the (202), (200), and (220) crystal facets of the nickel foam, respectively. These diffraction peaks exhibited strong agreement with the established pattern for nickel foam (PDF# 04-0850). In addition, the characteristic peaks for the complexes, appearing at 21.7°, 31.1°, 37.7°, 38.3°,44.3°, 49.7°, 50.1°, 54.5°, and 55.1°, also showed good agreement with the standard card of Ni_3S_2 (PDF#76-1870), further demonstrating the successful synthesis of Ni_3S_2 materials on nickel foam. Notably, the characteristic peaks of Mo did not

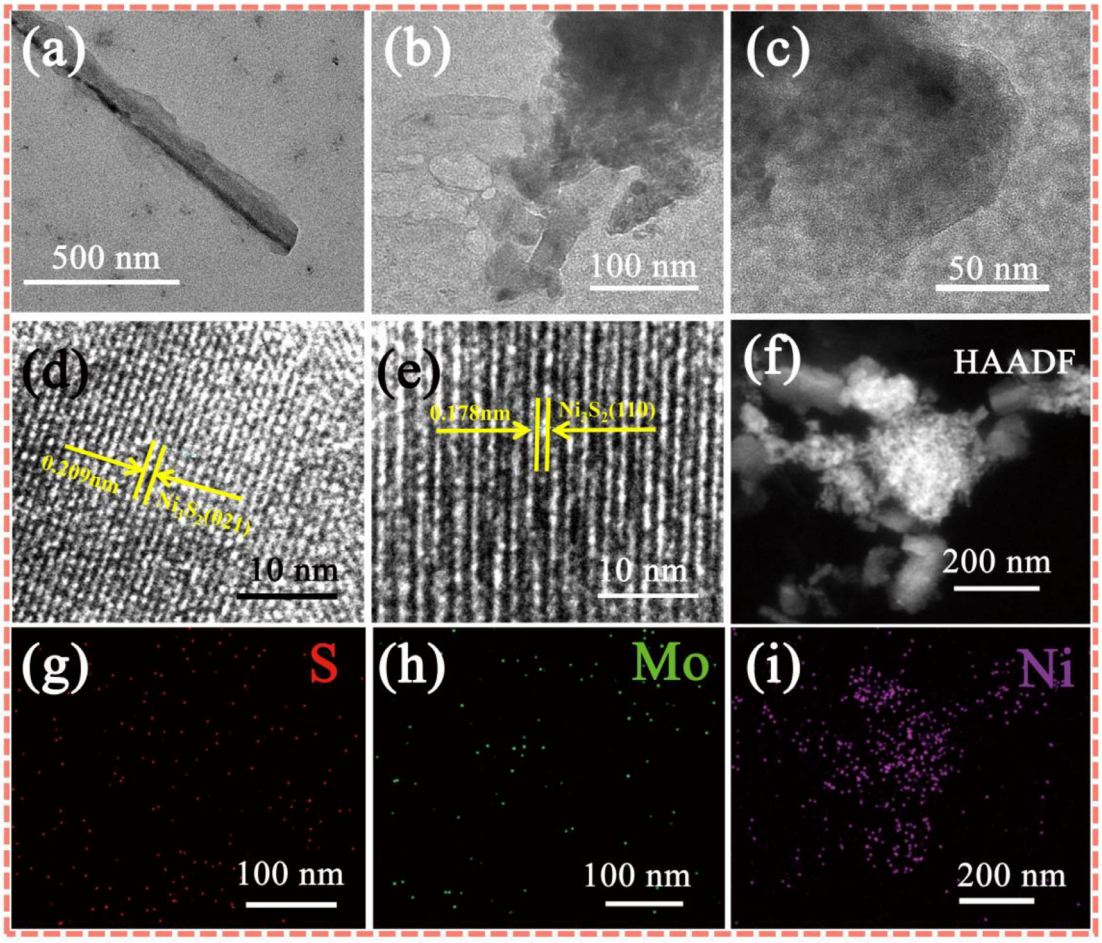

Fig. 3. (a)–(c) TEM images of Ni_3S_2-Mo-0.1 at different magnifications, (d) and (e) HRTEM images of Ni_3S_2-Mo-0.1 obtained by ultrasound, and (f)–(i) EDS mapping of Ni_3S_2-Mo-0.1.

appear in the XRD patterns of any of the Ni_3S_2-Mo complexes, owing to the low Mo doping content in the complexes.

As illustrated in Fig. 4(b), the XPS spectrum revealed characteristic sulfur peaks at 162.55 and 167.02 eV, which aligned with the $2p_{3/2}$ and $2p_{1/2}$ energy levels of sulfur, respectively. The energy position of the S 2p peak corresponds to the presence of S atoms in the −2 valence oxidation state, indicating that S ions are present in the material in their −2 valence form. In Fig. 4(c), we observed two significant peaks located at 855.35 and 872.81 eV, corresponding to the Ni $2p_{3/2}$ and Ni $2p_{1/2}$ orbitals, respectively. In the XPS spectra, the Ni 2p peak corresponds to the transfer of Ni electrons between the excited and ground states at the 2p energy level. Owing to the splitting of the 2p energy level of Ni, its positional energy is closely related to its chemical environment and valence state. In this experiment, the position of the Ni 2p peak indicated that the Ni ion existed in the +2 valence oxidation state, confirming the chemical state of Ni. Furthermore, in Fig. 4(d), two peak positions appeared at 231.67 and 235.22 eV, corresponding to the Mo $3d_{5/2}$ and Mo $3d_{3/2}$ orbitals, respectively. The positional energies of the 3d peaks of Mo indicated that the Mo ions in the sample existed in the +4 valence oxidation state. This demonstrates the successful doping of Mo into Ni_3S_2.

3.2. OER performance

The OER performance of Ni_3S_2-Mo and non-hydrothermalized Ni foam was analyzed by LSV in a standard three-electrode system of 1 M KOH, at 24–27 °C, and the analytical curves are shown in Fig. 5(a). The analysis was carried out in 1 M KOH solution at a rate of 0.01 mV s^{-1}. As shown in Fig. 5(a), Ni foam exhibits poor OER catalytic performance with an OER overpotential of 486 mV, at a current density of 10 mA cm^{-2} (applied to the material), whereas Ni_3S_2-Mo-0.1 of the prepared Ni_3S_2-Mo material exhibits optimal catalytic performance for OER under an overpotential of 279 mV, at a current density of 10 mA cm^{-2}. Compared to Ni form, Ni_3S_2-Mo-0.1 reduced the OER overpotential by 207 mV. In addition, the OER overpotential of Ni_3S_2-Mo-0.1 was 495 mV at a current density of 100 mA cm^{-2}, and its OER performance exceeded that of most non-precious metal catalysts studied so far. This excellent OER performance is mainly attributed to the introduction of Mo.

In addition, the OER kinetic properties of all samples were evaluated using the Tafel slope, as shown in Fig. 5(b); Ni_3S_2-Mo-0.1 had the lowest Tafel slope of 84.83 mV dec^{-1}. The Tafel slopes of Ni, Ni_3S_2-Mo-0, Ni_3S_2-Mo-0.05, and Ni_3S_2-Mo-0.15 were 198.89, 104.49, 85.96, and 86.45 mV dec^{-1}, respectively. Ni_3S_2-Mo-0.1 displays the smallest Tafel slope, implying superior kinetics for the OER. Furthermore, there is a strong correlation between the catalyst activity and ECSA of the material. CV curves of the materials were obtained at different scan rates, and the active sites of the catalysts were roughly compared using the electrochemical double-layer capacitance (C_{dl}) to calculate the ECSA (Fig. S2) [36–38]. As shown in Fig. 5(c), Ni_3S_2-Mo-0.1 had the most excellent C_{dl} value (13.4 mF cm^{-2}), which surpassed those of Ni_3S_2-Mo-0.05 (9.5 mF cm^{-2}), Ni_3S_2-Mo-0.15 (7.8 mF cm^{-2}), and Ni (1.5 mF cm^{-2}). This indicates that Ni_3S_2-Mo-0.1 has a larger catalytically active region and more active sites.

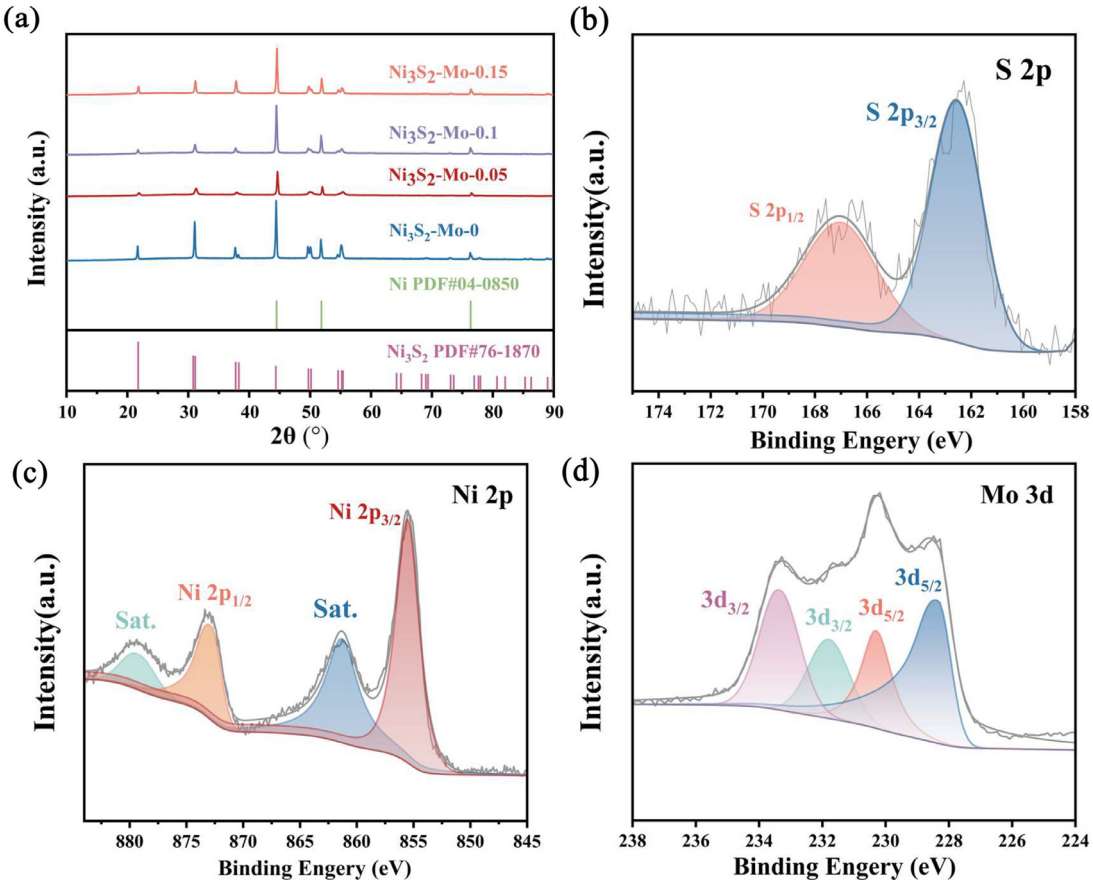

Fig. 4. (a) XRD spectra of various samples. High resolution XPS spectra of (b) S 2p, (c) Ni 2p, and (d) Mo 3d.

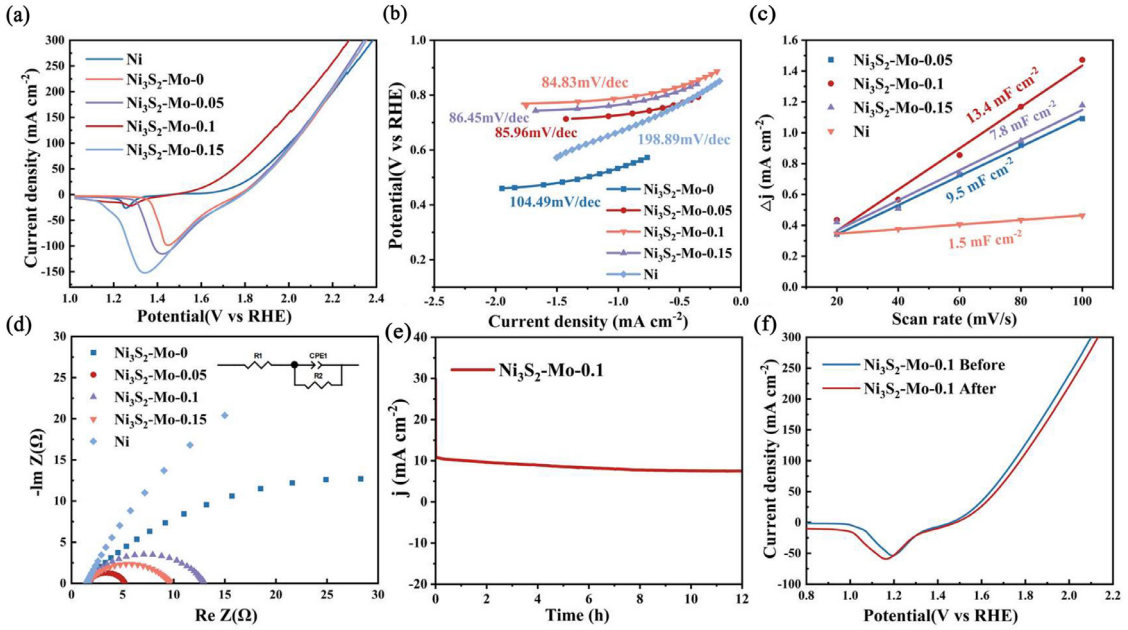

Fig. 5. Electrochemical measurements of Ni_3S_2-Mo. (a) OER curves of Ni_3S_2-Mo-0, Ni_3S_2-Mo-0.05, Ni_3S_2-Mo-0.1, Ni_3S_2-Mo-0.15, and Ni foam and the corresponding (b) OER Tafel slopes, (c) C_{dl} at different scan rates, (d) Nyquist plots, and (e) Ni_3S_2-Mo 0.1 *I-t* plots. (f) Comparison of the OER performance before and after stability tests.

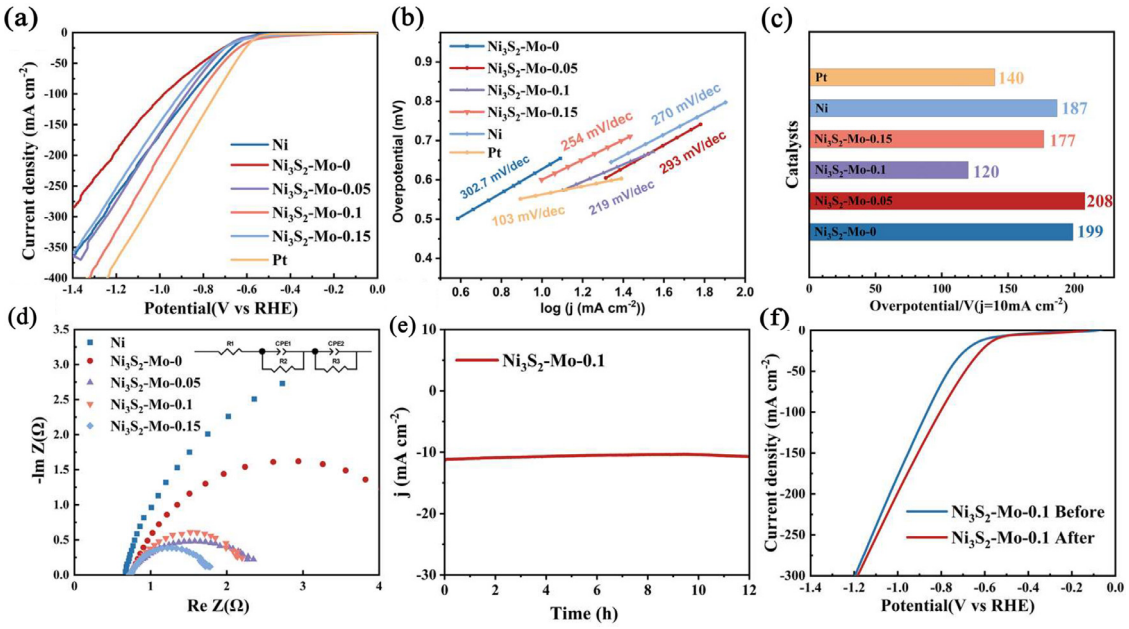

Fig. 6. Electrochemical measurements of Ni_3S_2-Mo. (a) HER curves for Ni_3S_2-Mo-0, Ni_3S_2-Mo-0.05, Ni_3S_2-Mo-0.1, Ni_3S_2-Mo-0.15, Ni foam, and Pt and the corresponding (b) HER Tafel slopes, (c) overpotentials at a current density of 10 mA cm^{-2}, and (d) Nyquist plots. (e) *I-t* plots of Ni_3S_2-Mo-0.1. (f) Comparison of the HER performance before and after the stability tests.

To investigate the electron transfer mechanism occurring at the electrode-electrolyte interface for each specimen, Nyquist diagrams spanning from 10 kHz to 0.01 Hz were generated through EIS (Fig. 5(d)). In Fig. 5(d), the charge transfer resistance (R_{ct}) is reflected by the diameter of the semicircular arcs, a key parameter for the Faraday kinetics at the reaction interface [39,40]. The R_{ct} of Ni_3S_2-Mo-0.1 was lower than that of the other samples. This suggests that electron transfer during the OER process for Ni_3S_2-Mo-0.1 occurs with remarkable ease.

In addition, electrochemical stability is an important factor in evaluating the performance of electrocatalysts [41]. We performed a constant voltage test on Ni_3S_2-Mo-0.1 for 12 h. Fig. 5(e) shows that the operating current density of Ni_3S_2-Mo-0.1 remained constant. The initial activity was maintained at 93.33% after 12 h of catalysis. The OER performance of Ni_3S_2-Mo-0.1 was then tested again (Fig. 5(f)). The results demonstrated reductions of 23 and 27 mV in the OER overpotential at current densities of 10 and 100 mA cm^{-2}, respectively. This underscores the effective preservation of catalyst performance after the stability assessment.

3.3. HER performance

Under the same test conditions, several sets of samples were exposed to a freshly prepared 1 M KOH solution at a scan rate of 0.01 mV s^{-1}, and linear voltametric scans were performed to analyze their alkaline HER properties. As shown in Fig. 6(a), the HER overpotential of Ni_3S_2-Mo-0.1 was 120 mV at a current density of 10 mA cm^{-2}, while that of the Ni foam electrode was 187 mV. Compared to other materials, Ni_3S_2-Mo-0.1 showed a higher overpotential than Ni foam, Ni_3S_2-Mo-0, Ni_3S_2-Mo-0.05, and Ni_3S_2-Mo-0.15 (67, 79, 88, and 57 mV, respectively). In addition, the HER overpotential of the Ni_3S_2-Mo-0.1 electrode was 396 mV at a current density of 100 mA cm^{-2}. Ni_3S_2-Mo-0.1 has such excellent HER properties because of the introduction of Mo atoms. The introduction of a single Mo atom played a key role in improving the HER performance of the electrode; this can be attributed to the fine-tuning of the Mo atoms, which improved the electrical conductivity of the material (Fig. 6(d)) [42].

In the HER, the kinetic path of the surface is determined by the Tafel slope. As shown in Fig. 6(d), among the evaluated samples, the Ni_3S_2-Mo-0.1 core-shell configuration demonstrates the lowest Tafel slope of 219 mV dec^{-1}. In contrast, the Tafel slopes of the Ni foam, Ni_3S_2-Mo-0, Ni_3S_2-Mo-0.05, and Ni_3S_2-Mo-0.15 were 270, 302.7, 293, and 254 mV dec^{-1}, respectively. By comparing the Tafel slopes of the above samples, it can be concluded that the introduction of Mo atoms improves the HER kinetics at the catalyst surface.

The Ni_3S_2-Mo-0.1 electrode was tested at constant voltage for 12 h (Fig. 6(e)), and the results showed that the operating current density of Ni_3S_2-Mo-0.1 was maintained at a good and stable value. The initial activity remained at 94.9% after the catalytic process. We then tested the HER performance of Ni_3S_2-Mo-0.1 again (Fig. 6(f)). The findings demonstrated a reduction of 44 and 60 mV in the HER overpotential at current densities of 10 and 100 mA cm^{-2}, respectively. This indicates that the performance of the catalyst further improved after the stability test, suggesting that the Ni_3S_2-Mo-0.1 electrode underwent a certain activation process during the stability test.

3.4. Overall water splitting

The Ni_3S_2-Mo-0.1 catalyst exhibited good catalytic activity for HER and OER in a 1.0 M KOH solution. Therefore, we applied it to a dual system of electrochemical water splitting for hydrogen and oxygen production. Tests showed that Ni_3S_2-Mo-0.1||Ni_3S_2-Mo-0.1 required only 1.62 V for overall water splitting (Fig. 7(e)). Fig. 7(a) shows the hydrogen- and oxygen-collection devices. After a certain period of gas collection, the experimental results were recorded, and the results are presented in Fig. 7(b). The actual volume of oxygen collected was less than the theoretical volume, probably owing to the higher solubility of oxygen in water.

At the end of the overall water splitting, we performed an electrode durability test on the material (Figs. 7(c)(d)), which showed that there was almost no degradation of the current density profile of Ni_3S_2-Mo-0.1 during the 12 h stability test. In addition, after the stability test, the performance of the electrode in overall water splitting was tested again (Figs. 7(f)(g)), and these outcomes were in accordance with earlier experiments. After the stability test, Ni_3S_2-Mo-0.1 underwent an activation process, and the electrode improved its performance in both hydrogen and oxygen production. This confirms that the Ni_3S_2-Mo-0.1

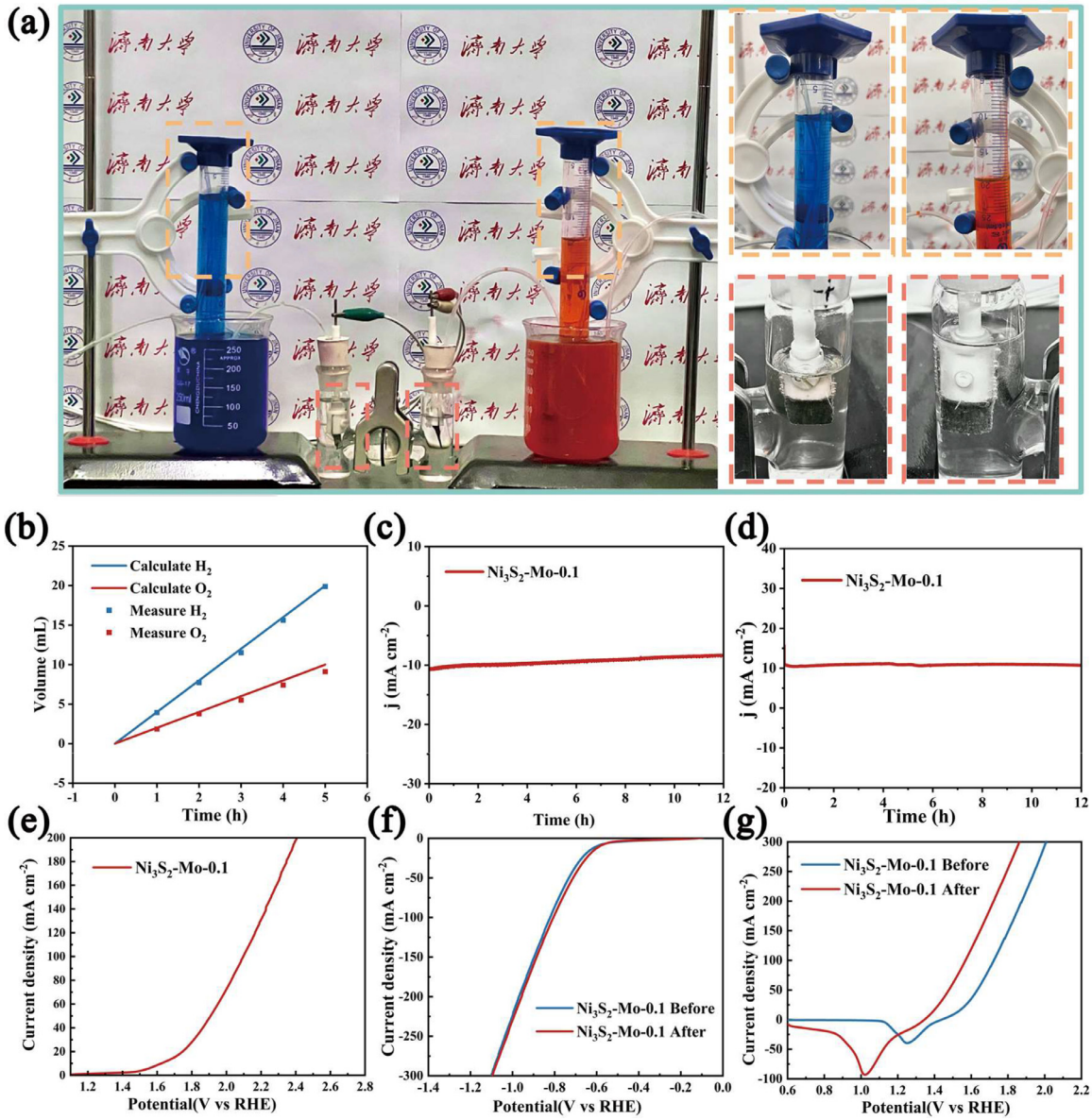

Fig. 7. (a) Ni_3S_2-Mo-0.1||Ni_3S_2-Mo-0.1 double-electrodes system for overall water splitting and gas collection. (b) Variation of the actual gas collection volume and theoretical calculation volume with respect to time. (c) HER *I-t* plots of Ni_3S_2-Mo-0.1. (d) OER *I-t* plots of Ni_3S_2-Mo-0.1. (e) Polarization curves of Ni_3S_2-Mo-0.1. (f) Comparison of the HER performance before and after the stability test. (g) Comparison of the OER performance before and after the stability test.

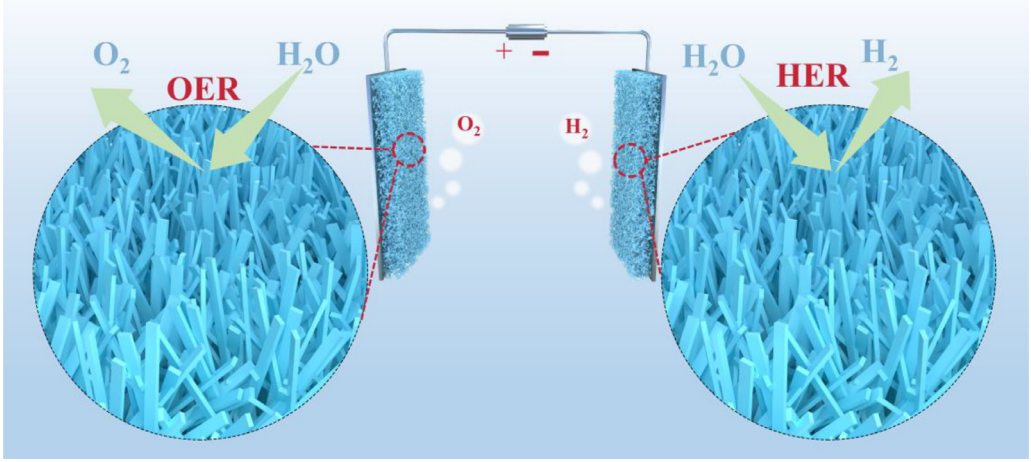

Fig. 8. Schematic diagram of the overall water splitting.

catalyst has both excellent performance and superior stability. Furthermore, we conducted SEM and XRD tests to explore the alterations in the material composition and morphology of Ni_3S_2-Mo-0.1 after the comprehensive water splitting and stability assessments.

As shown in Fig. S3, the number of 1D needle-like crystal structures on the surface of the Ni_3S_2-Mo-0.1 electrocatalysts partially decreased after the overall water splitting and stability tests, indicating that these needle-like crystals with a one-dimensional structure constitute the reactive segment in the electrochemical process. Compared with the initial SEM images, the morphology remained unchanged, and the large number of retained 1D needle-like crystals confirmed the excellent stability of Ni_3S_2-Mo-0.1.

As shown in Fig. 8, Ni_3S_2-Mo-0.1 electrocatalyst was synthesized using a one-step hydrothermal method. Its unique 1D needle-like structure provides numerous active regions. Furthermore, the modification of the catalyst with Mo atoms improved the overpotential for hydrogen and oxygen production. In addition, the catalyst exhibits good corrosion resistance and an extended lifespan.

4. Conclusion

In summary, in this study, we successfully prepared a 1D needle-like efficient bifunctional electrocatalyst Ni_3S_2-Mo-0.1, by doping molybdenum obtained via a one-step hydrothermal method into nickel sulfide (Ni_3S_2). The obtained Ni_3S_2-Mo-0.1 catalysts exhibited excellent HER and OER performances in 1.0 M KOH solution. The electrochemical analyses showed that the obtained 1D needle-like structure of the Ni_3S_2-Mo-0.1 sample exhibited HER and OER overpotentials of 120 and 279 mV, respectively, at a current density of 10 mA cm^{-2}. At a current density of 100 mA cm^{-2}, the HER and OER overpotential were 396 and 495 mV, respectively. The electrocatalytic performance of Ni_3S_2-Mo-0.1||Ni_3S_2-Mo-0.1 required only a cell voltage of 1.62 V to achieve overall water splitting. The introduction of Mo atoms enlarged the electrocatalytically active sites and increased the catalyst conductivity, whereas the coupling between Ni_3S_2 and Mo atom interfaces increased the internal electric field and optimized the electronic structure [43–46]. Thus, the effects of modulating the nickel sulfide interface with molybdenum atom on the microstructure of the catalysts, hydrogen precipitation performance of electrolytic water, and double layer capacitance were thoroughly investigated. This study can serve as a valuable guide for achieving efficient alkaline hydrogen production and overall water splitting.

Declaration of Competing Interest

We declare that we do not have any commercial or associative interest that represents a conflict of interest in connection with the work submitted.

CRediT authorship contribution statement

Junjie Huang: Data curation, Writing – original draft. **Yupeng Xing:** Data curation, Writing – original draft. **Jinzhao Huang:** Resources. **Fei Li:** Resources. **Gang Zhao:** Formal analysis, Funding acquisition, Investigation, Methodology, Resources, Writing – original draft, Writing – review & editing. **Xingmin Yu:** Methodology. **Binxun Li:** Project administration. **Xinran Zhang:** Project administration.

Acknowledgement

This work was supported by the National Natural Science Foundation of China (No. 51802177) and the Joint Funds of the National Natural Science Foundation of China (No. U22A20140) and State Key Laboratory of Powder Metallurgy, Central South University, Changsha, China. All authors contributed to the preparation, characterization, and analysis of the structures and performance of the materials. All the authors discussed the results and commented on the manuscript.

Supplementary materials

Supplementary material associated with this article can be found, in the online version, at doi:10.1016/j.chphma.2023.11.001.

References

[1] R. Chen, T. Zhao, X. Zhang, L. Li, F. Wu, Advanced cathode materials for lithium-ion batteries using nanoarchitectonics, Nanoscale Horiz. 1 (2016) 423–444, doi:10.1039/c6nh00016a.
[2] Z. Qiu, Y. Yun, M. He, L. Wang, Recent developments in ion conductive membranes for CO_2 electrochemical reduction, Chem. Eng. J. 456 (2023) 140942, doi:10.1016/j.cej.2022.140942.
[3] F.L. Formal, W.S. Bourée, M.S. Prévot, K. Sivula, Challenges towards economic fuel generation from renewable electricity: The need for efficient electro-catalysis, Chimia 69 (2015) 789, doi:10.2533/chimia.2015.789.
[4] Y. Pang, M.N. Uddin, W. Chen, S. Javaid, E. Barker, Y. Li, A. Suvorova, M. Saunders, Z. Yin, G. Jia, Photocatalysts: Colloidal single-layer photocatalysts for methanol-storable solar H_2 fuel, Adv. Mater. 31 (2019) 1970348, doi:10.1002/adma.201970348.
[5] N. Han, P. Liu, J. Jiang, L. Ai, Z. Shao, S. Liu, Recent advances in nanostructured metal nitrides for water splitting, J. Mater. Chem. A 6 (2018) 19912–19933, doi:10.1039/c8ta06529b.
[6] D. Chen, H. Zhang, Y. Li, Y. Pang, Z. Yin, H. Sun, L. Zhang, S. Wang, M. Saunders, E. Barker, G. Jia, Spontaneous formation of noble- and heavy-metal-free alloyed semiconductor quantum rods for efficient photocatalysis, Adv. Mater. 30 (2018) 1803351, doi:10.1002/adma.201803351.
[7] A.H. Alshammari, M. Alshammari, S. Alhassan, K. Alshammari, T. Alotaibi, T.A.M. Taha, MoO_3/S@g-C_3N_4 nanocomposite structures: Synthesis, characterization, and hydrogen catalytic performance, Nanomaterials 13 (2023) 820, doi:10.3390/nano13050820.
[8] J. Shah, S. Jain, A. Shukla, R. Gupta, R.K. Kotnala, A facile non-photocatalytic technique for hydrogen gas production by hydroelectric cell, Int. J. Hydrogen Energy 42 (2017) 30584–30590, doi:10.1016/j.ijhydene.2017.10.105.
[9] X. Du, C. Huang, X. Zhang, Surface modification of a Co_9S_8 nanorods with $Ni(OH)_2$ on nickel foam for high water splitting performance, Int. J. Hydrogen Energy 44 (2019) 19953–19966, doi:10.1016/j.ijhydene.2019.06.003.
[10] S. Wang, A. Lu, C.J. Zhong, Hydrogen production from water electrolysis: Role of catalysts, Nano Convergence 8 (2021) 4, doi:10.1186/s40580-021-00254-x.
[11] M. Nemiwal, V. Gosu, T.C. Zhang, D. Kumar, Metal organic frameworks as electrocatalysts: Hydrogen evolution reactions and overall water splitting, Int. J. Hydrogen Energy 46 (2021) 10216–10238, doi:10.1016/j.ijhydene.2020.12.146.
[12] W. Wang, X. Xu, W. Zhou, Z. Shao, Recent progress in metal-organic frameworks for applications in electrocatalytic and photocatalytic water splitting, Adv. Sci. 4 (2017) 1600371, doi:10.1002/advs.201600371.
[13] Y. Zhou, R. Abazari, J. Chen, M. Tahir, A. Kumar, R.R. Ikreedeegh, E. Rani, H. Singh, A.M. Kirillov, Bimetallic metal–organic frameworks and MOF-derived composites: Recent progress on electro- and photoelectrocatalytic applications, Coordin. Chem. Rev. 451 (2022) 214264, doi:10.1016/j.ccr.2021.214264.
[14] L. Xu, X. Huang, S. Xiong, Z. Wang, B. Peng, Z. Ma, J. Zeng, H. Li, S. Tang, Z. Li, L.L. Wang, Type-II CeO_2(111)/hBN vdW heterojunction for enhanced photocatalytic hydrogen evolution: A first principles study, Int. J. Hydrogen Energy 46 (2021) 25060–25069, doi:10.1016/j.ijhydene.2021.05.044.
[15] S. Javaid, X. Xu, W. Chen, J. Chen, H.Y. Hsu, S. Wang, X. Yang, Y. Li, Z. Shao, F. Jones, G. Jia, Ni^{2+}/Co^{2+} doped Au-Fe_7S_8 nanoplatelets with exceptionally high oxygen evolution reaction activity, Nano Energy 89 (2021) 106463, doi:10.1016/j.nanoen.2021.106463.
[16] Y. Xie, J. Cai, Y. Wu, X. Hao, Z. Bian, S. Niu, X. Yin, Z. Pei, D. Sun, Z. Zhu, Z. Lu, D. Niu, G. Wang, Atomic disorder enables superior catalytic surface of Pt-based catalysts for alkaline hydrogen evolution, ACS Mater. Lett. 3 (2021) 1738–1745, doi:10.1021/acsmaterialslett.1c00559.
[17] Y. Pei, B. Rezaei, X. Zhang, Z. Li, H. Shen, M. Yang, J. Wang, Interface catalysis by Pt nanocluster@Ni_3N for bifunctional hydrogen evolution and oxygen evolution, Mater. Chem. Front. 4 (2020) 2665–2672, doi:10.1039/d0qm00326c.
[18] J. Dong, Y. Lu, X. Tian, F. Zhang, S. Chen, W. Yan, H. He, Y. Wang, Y. Zhang, Y. Qin, M. Sui, X. Zhang, X. Fan, Genuine active species generated from fe3n nanotube by synergistic coni doping for boosted oxygen evolution catalysis, Small 16 (2020) 2003824, doi:10.1002/smll.202003824.
[19] K. Srinivas, Y. Chen, X. Wang, B. Wang, M. Karpuraranjith, W. Wang, Z. Su, W. Zhang, D. Yang, Constructing Ni/NiS heteronanoparticle-embedded metal–organic framework-derived nanosheets for enhanced water-splitting catalysis, ACS Sustain. Chem. Eng. 9 (2021) 1920–1931, doi:10.1021/acssuschemeng.0c08543.
[20] X. Li, W. Wang, F. Dong, Z. Zhang, L. Han, X. Luo, J. Huang, Z. Feng, Z. Chen, G. Jia, T. Zhang, Recent advances in noncontact external-field-assisted photocatalysis: From fundamentals to applications, ACS Catal 11 (2021) 4739–4769, doi:10.1021/acscatal.0c05354.
[21] S. Guan, X. Fu, Z. Lao, C. Jin, Z. Peng, NiS–MoS_2 hetero-nanosheet array electrocatalysts for efficient overall water splitting, Sustain. Energ. Fuels. 3 (2019) 2056–2066, doi:10.1039/c9se00228f.
[22] Z. Chen, X. Liu, P. Xin, H. Wang, Y. Wu, C. Gao, Q. He, Y. Jiang, Z. Hu, S. Huang, Interface engineering of NiS@MoS_2 core-shell microspheres as an efficient catalyst for hydrogen evolution reaction in both acidic and alkaline medium, J. Alloy Compd. 853 (2021) 157352, doi:10.1016/j.jallcom.2020.157352.

[23] S. Yang, H. Guan, Y. Zhong, J. Quan, N. Luo, Q. Gao, Y. Xu, F. Peng, S. Zhang, Y. Fang, CdS@Ni_3S_2 for efficient and stable photo-assisted electrochemical (P-EC) overall water splitting, Chem. Eng. J. 405 (2021) 126231, doi:10.1016/j.cej.2020.126231.
[24] H. Qin, B. Zhang, Y. Pan, X. Wang, L. Diao, J. Chen, J. Wu, E. Liu, J. Sha, L. Ma, N. Zhao, Accelerating water dissociation kinetics on Ni_3S_2 nanosheets by P-induced electronic modulation, J. Catal. 381 (2020) 493–500, doi:10.1016/j.jcat.2019.11.018.
[25] G. Zhai, D. Xu, S. Zhang, Z. Xue, H. Su, Q. Yu, H. Wang, X. Lin, Y. Lin, L. Sun, X. Li, J. Chen, Isoelectric Si heteroatoms as electron traps for N_2 fixation and activation, Adv. Funct. Mater. 30 (2020) 2005779, doi:10.1002/adfm.202005779.
[26] L. Zhang, Y. Jia, X. Yan, X. Yao, Activity origins in nanocarbons for the electrocatalytic hydrogen evolution reaction, Small 14 (2018) 1800235, doi:10.1002/smll.201800235.
[27] C.W. Chen, C.Y. Chiang, Molybdenum-containing amorphous metal oxide catalysts for oxygen evolution reaction, Int. J. Hydrogen Energy 42 (2017) 29773–29780, doi:10.1016/j.ijhydene.2017.10.009.
[28] H. Noh, Y. Yang, X. Zhang, T.A. Goetjen, Z.H. Syed, Z. Lu, S. Ahn, O.K. Farha, J.T. Hupp, Single-Site, single-metal-atom, heterogeneous electrocatalyst: Metal-organic-framework supported molybdenum sulfide for redox mediator-assisted hydrogen evolution reaction, ChemElectroChem 7 (2020) 509–516, doi:10.1002/celc.201901650.
[29] Y. Bao, M. Yang, S.J.R. Tan, Y.P. Liu, H. Xu, W. Liu, C.T. Nai, Y.P. Feng, J. Lu, K.P. Loh, Substoichiometric molybdenum sulfide phases with catalytically active basal planes, J. Am. Chem. Soc. 138 (2016) 14121–14128, doi:10.1021/jacs.6b09042.
[30] M. Zheng, B. Cao, J. Liu, K. Shi, Y. Zhang, H. Wang, Facile synthesis of ordered mesoporous molybdenum carbide electrocatalysts for high-performance hydrogen evolution reaction, Electroanalysis 35 (2023) e202200519, doi:10.1002/elan.202200519.
[31] F. Wang, W. Ueda, J. Xu, Detection and measurement of surface electron transfer on reduced molybdenum oxides (MoO_x) and catalytic activities of Au/MoO_x, Angew. Chem. 124 (2012) 3949–3953, doi:10.1002/ange.201105922.
[32] N. Mahmood, Y. Yao, J. Zhang, L. Pan, X. Zhang, J. Zou, Electrocatalysts for hydrogen evolution in alkaline electrolytes: Mechanisms, challenges, and prospective solutions, Adv. Sci. 5 (2017) 1700464, doi:10.1002/advs.201700464.
[33] L. Yang, J. Shui, L. Du, Y. Shao, J. Liu, L. Dai, Z. Hu, Carbon-based metal-free ORR electrocatalysts for fuel cells: Past, present, and future, Adv. Mater. 31 (2019) 1804799, doi:10.1002/adma.201804799.
[34] R. Sharma, S. Gyergyek, S.M. Andersen, Critical thinking on baseline corrections for electrochemical surface area (ECSA) determination of Pt/C through H-adsorption/H-desorption regions of a cyclic voltammogram, Appl. Catal. B: Environ. 311 (2022) 121351, doi:10.1016/j.apcatb.2022.121351.
[35] S.S. Jeon, P.W. Kang, M. Klingenhof, H. Lee, F. Dionigi, P. Strasser, Active surface area and intrinsic catalytic oxygen evolution reactivity of nife LDH at reactive electrode potentials using capacitances, ACS Catal. 13 (2023) 1186–1196, doi:10.1021/acscatal.2c04452.
[36] S. Watzele, P. Hauenstein, Y. Liang, S. Xue, J. Fichtner, B. Garlyyev, D. Scieszka, F. Claudel, F. Maillard, A.S. Bandarenka, Determination of electroactive surface area of Ni-, Co-, Fe-, and Ir-based oxide electrocatalysts, ACS Catal. 9 (2019) 9222–9230, doi:10.1021/acscatal.9b02006.
[37] J. Speder, A. Zana, I. Spanos, J.J.K. Kirkensgaard, K. Mortensen, M. Hanzlik, M. Arenz, Comparative degradation study of carbon supported proton exchange membrane fuel cell electrocatalysts–The influence of the platinum to carbon ratio on the degradation rate, J. Power Sources 261 (2014) 14–22, doi:10.1016/j.jpowsour.2014.03.039.
[38] J. Kim, H. Kim, S.K. Kim, S.H. Ahn, Electrodeposited amorphous Co–P–B ternary catalyst for hydrogen evolution reaction, J. Mater. Chem. A 6 (2018) 6282–6288, doi:10.1039/c7ta11033b.
[39] X. Yang, X. Li, Y. Wang, C. Ye, Z. Du, H. Yu, J. Liu, L. Chen, B. Su, Efficient etching of oxygen-incorporated molybdenum disulfide nanosheet arrays for excellent electrocatalytic hydrogen evolution, Appl. Surf. Sci. 491 (2019) 245–255, doi:10.1016/j.apsusc.2019.06.153.
[40] T. Mohammadi, Y. Ghayeb, T. Sharifi, M.M. Momeni, RuO_2 photodeposited on W-doped and Cr-doped TiO_2 nanotubes with enhanced photoelectrochemical water splitting and capacitor properties, New J. Chem. 44 (2020) 2339–2349, doi:10.1039/c9nj03322j.
[41] C.P. Lo, G. Wang, A. Kumar, V. Ramani, TiO_2–RuO_2 electrocatalyst supports exhibit exceptional electrochemical stability, Appl. Catal. B: Environ. 140 (2013) 133–140, doi:10.1016/j.apcatb.2013.03.039.
[42] W. Huang, Y. Yuan, K. Wang, Q. Cao, Y. Zhao, X. Sun, R. Ding, P. Gao, W. Cai, E. Liu, Tuning interface density and electronic structure of NiS/Ni_3S_4 by Mo, Co co-doping for efficient urea electrooxidation reaction, J. Electroanal. Chem. 911 (2022) 116242, doi:10.1016/j.jelechem.2022.116242.
[43] Y. Wang, D. Wang, Y. Li, Atom-level interfacial synergy of single-atom site catalysts for electrocatalysis, J. Energy Chem. 65 (2022) 103–115, doi:10.1016/j.jechem.2021.05.038.
[44] H. Jin, X. Liu, Y. Jiao, A. Vasileff, Y. Zheng, S.Z. Qiao, Constructing tunable dual active sites on two-dimensional C_3N_4@MoN hybrid for electrocatalytic hydrogen evolution, Nano Energy 53 (2018) 690–697, doi:10.1016/j.nanoen.2018.09.046.
[45] S. Lv, Y. Deng, Z. Fu, M. Wang, Z. Xiao, B. Li, L. Wang, Carbon-quantum-dots-involved Fe/Co/Ni phosphide open nanotubes for high effective seawater electrocatalytic decomposition, Appl. Catal. B: Environ. 326 (2023) 122403, doi:10.1016/j.apcatb.2023.122403.
[46] H. Zhang, Y. Wu, X. Wang, C. Li, Z. Xiao, Y. Liu, Y. Deng, Z. Li, L. Wang, The construction of defect-rich CoP@CoP@$(Co/Ni)_2P$ triple-shell hollow nanospheres with boosted electrocatalytic hydrogen evolution performances over a wide pH range, Chem.Eng. J. 463 (2023), doi:10.1016/j.cej.2023.142448.